nature catalysis

Article

https://doi.org/10.1038/s41929-024-01148-x

Visualizing the structural evolution of individual active sites in MoS_2 during electrocatalytic hydrogen evolution reaction

Received: 3 March 2023

Accepted: 15 March 2024

Teng-Xiang Huang[1,5], Xin Cong[2,5], Si-Si Wu[1], Jiang-Bin Wu[2], Yi-Fan Bao[1], Mao-Feng Cao[1], Liwen Wu[1], Miao-Ling Lin[2], Xiang Wang[1,3] ✉, Ping-Heng Tan[2,4] ✉ & Bin Ren[1,3] ✉

Understanding the structural evolution of individual active sites during a reaction is a long-standing target in surface science and catalysis. It is still challenging to precisely characterize in situ the intrinsic nature and evolution of the active site because the active site is too small for characterization techniques to decipher the local properties. Here we used electrochemical tip-enhanced Raman spectroscopy to monitor the geometric and electronic evolution of individual active sites of MoS_2 during the hydrogen evolution reaction. Reconstruction regions of 40 nm with varied lattice and electron density from the edge to the nearby basal plane were observed during the hydrogen evolution reaction. We further revealed the progressive generation of active sites during the activation process. The synergistic reconstruction around edge due to the lattice deformation reduces the activation energy barriers and promotes the electrocatalytic reaction. These discoveries offer insights into our understanding of the active site and its dynamics during electrocatalysis.

With the growing demand for greener energy, electrochemistry has been receiving increasing attention in recent years because it is key to the development of renewable energy storage and conversion from intermittent sources. The activity of electrochemical devices is mainly governed by nanoscale active sites with specific geometric and electronic structures[1,2]. Recent works have shown that some materials evolve during the electrochemical reaction[3,4], different from the conventional understanding of catalysts with unchanged and defined structures. However, it is still very challenging to precisely characterize in situ the structural evolution of active sites during a reaction. Most characterization techniques can only obtain the average information contributed by all active sites in the sampling region and are unable to decipher the specific structure and activity of local individual active sites, let alone reveal the intrinsic nature of the active site, including how it forms and evolves.

Great endeavours have been made to develop in situ microscopic techniques with a high spatial resolution to characterize the structure of individual active sites and elucidate their roles in accelerating chemical reactions. For example, catalytically active sites have been accurately identified by single-molecule fluorescence imaging[5] enabled by superlocalization and by electrochemical scanning tunnelling microscope (EC-STM)[6] using the tunnelling current noise as the signal.

---

[1] State Key Laboratory of Physical Chemistry of Solid Surfaces, Collaborative Innovation Center of Chemistry for Energy Materials (iChEM), MOE Key Laboratory of Spectrochemical Analysis & Instrumentation, Department of Chemistry, College of Chemistry and Chemical Engineering, Xiamen University, Xiamen, China. [2] State Key Laboratory of Superlattices and Microstructures, Institute of Semiconductors, Chinese Academy of Sciences, Beijing, China. [3] Innovation Laboratory for Sciences and Technologies of Energy Materials of Fujian Province (IKKEM), Xiamen, China. [4] Center of Materials Science and Optoelectronics Engineering & CAS Center of Excellence in Topological Quantum Computation, University of Chinese Academy of Sciences, Beijing, China. [5] These authors contributed equally: Teng-Xiang Huang, Xin Cong. ✉e-mail: wangxiang@xmu.edu.cn; phtan@semi.ac.cn; bren@xmu.edu.cn

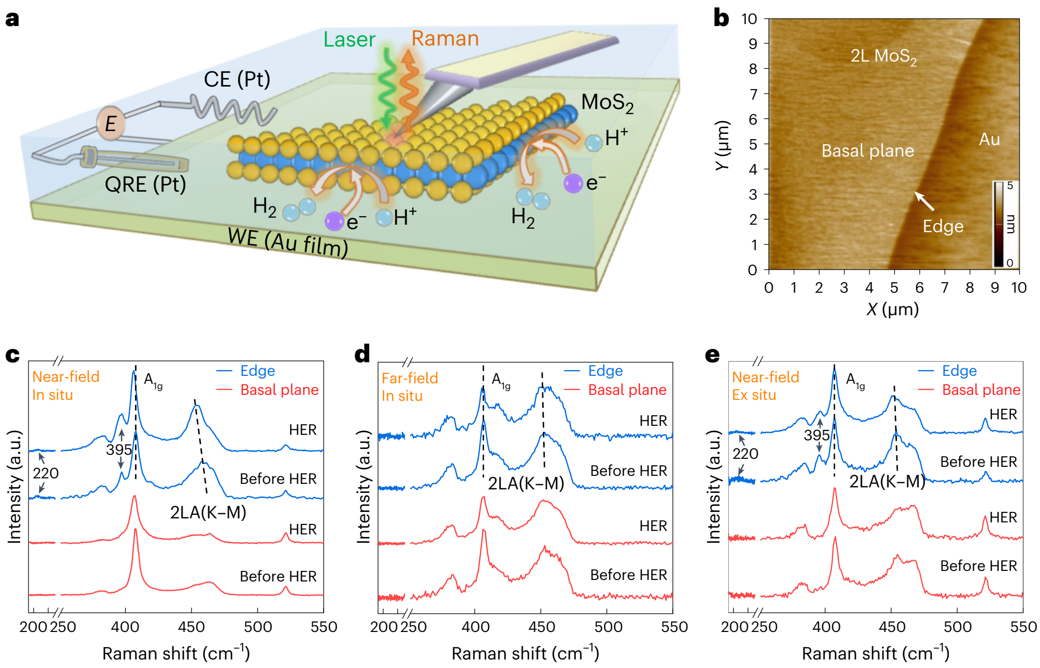

Fig. 1 | EC-TERS study of active and inactive sites in ultrathin MoS_2 during the HER. a, Schematic of the experimental set-up. CE, counterelectrode; WE, working electrode. **b**, AFM image of the mechanically exfoliated bilayer MoS_2 on an atomically smooth gold film. The inset colour scale bar denotes the topographic height. **c**,**d**, EC-TERS (**c**) and confocal Raman (**d**) spectra of edges and basal planes before (0.05 V versus RHE) and during HER (−0.3 V versus RHE). **e**, Ex situ TERS spectra of edges and basal planes before and after HER at −0.3 V versus RHE. The intensities were normalized with the A_{1g} peak of spectra before the HER for comparison. Note that spectra in **c** and **e** are the original TERS spectra without background subtraction of the far-field signal.

Transmission electron microscopy (TEM)[4] has been used to observe the morphological change of active sites in situ. The reaction dynamics at active sites have been uncovered by single-molecule fluorescence imaging[7] from the on–off fluorescence signals and by scanning electrochemical cell microscopy[3] from the local reaction current. However, it is still a great challenge to monitor the evolution of geometric and electronic structures of active sites that indeed determine the catalytic performance and establish accurate structure–activity relationships. The emergence of electrochemical tip-enhanced Raman spectroscopy (EC-TERS)[8,9], which is capable of simultaneously providing surface morphology and fingerprint information with a spatial resolution of several nanometres or less, offers an promising opportunity to address the above issues[10–12].

In this work, we used EC-TERS to monitor in situ the geometric and electronic evolution of catalytically active sites during the hydrogen evolution reaction (HER) with nanometre spatial resolution. We adopted atomically thin two-dimensional layered molybdenum disulfide (MoS_2) with a well-defined structure as the model catalyst. MoS_2 is a promising non-noble metal catalyst alternative to platinum for the HER[13], and the edge or vacancy defect sites, other than the basal plane, are considered to be active for the HER[14,15]. Using Raman peaks sensitive to the lattice symmetry and electron density, we observed reconstruction regions of 40 nm with varied lattice and electron density from the edge sites to the nearby basal plane during the HER. We further monitored the geometric and electronic properties evolution of different surface sites, including active and inactive sites, and observed the progressive generation of active sites during the electrochemical activation process, which have not been achieved before. The synergistic reconstruction around active edges as a result of lattice deformation reduces the activation energy barriers and promotes the electrocatalytic reaction. These discoveries offer insights into our understanding of the active site and its dynamics during electrocatalytic processes, which may guide the rational design of surface sites to realize high-performance catalysis.

Results

Advantage of EC-TERS in the study of active sites

Figure 1a shows a schematic of the set-up to measure the Raman signals of catalytically inactive (that is, basal plane) and active (that is, edge) sites in MoS_2 flakes during the HER by EC-TERS. We first transferred the mechanically exfoliated bilayer (2L) MoS_2 flakes onto an atomically smooth gold film as the sample[16–18], followed by far-field photoluminescence measurement to identify the layer thickness (Supplementary Fig. 1). Next, an EC-TERS cell was assembled with the sample-loaded gold film as the working electrode, a platinum black ring as the counterelectrode and a platinum wire as the quasi-reference electrode (QRE)[19]. The electrode potential of the platinum with respect to the reversible hydrogen electrode (RHE) can be determined by $E_{\text{vs Pt}} = E_{\text{vs RHE}} - 0.649$ V. The EC-TERS study of MoS_2 during the HER in 0.5 M H_2SO_4 was carried out on a top-illumination EC-AFM-TERS with a SiO_2-coated gold tip[19,20]. An atomic force microscopy (AFM) image of the sample (Fig. 1b) was measured to identify different structural features on the surface. Finally, EC-TERS signals were measured at either a single point or in a line-scan manner.

Figure 1c shows the EC-TERS spectra of the basal plane and edge of 2L MoS_2 at 0.05 V versus RHE (before HER) and −0.3 V versus RHE (intense HER) (hydrogen evolution at the edge of MoS_2 starts at −0.15 V versus platinum[21]; Supplementary Note 1), respectively. Two defect-induced Raman modes (220 cm^{-1}, longitudinal acoustic (LA) phonons[16,22]; 395 cm^{-1}, the combination of the LA and transverse acoustic (TA) phonons, LA(M) + TA(M)[16]) can only be detected at the edge, indicating the advantage of the high spatial resolution (~7.3 nm, Supplementary Fig. 18) of EC-TERS. When the potential is changed from 0.05 V to −0.3 V versus RHE, the feature of the EC-TERS spectra from the basal plane almost remains unchanged except for slight intensity weakening and downshift of peak position due to the accumulation of electrons[23], which can also be observed in the EC-Raman spectra of monolayer MoS_2 (Supplementary Fig. 2). However, Raman peaks of the edge, in particular the A_{1g} mode (405 cm^{-1}) and 2LA(K–M) mode (450 cm^{-1}) from the van Hove singularity in the vibrational density of

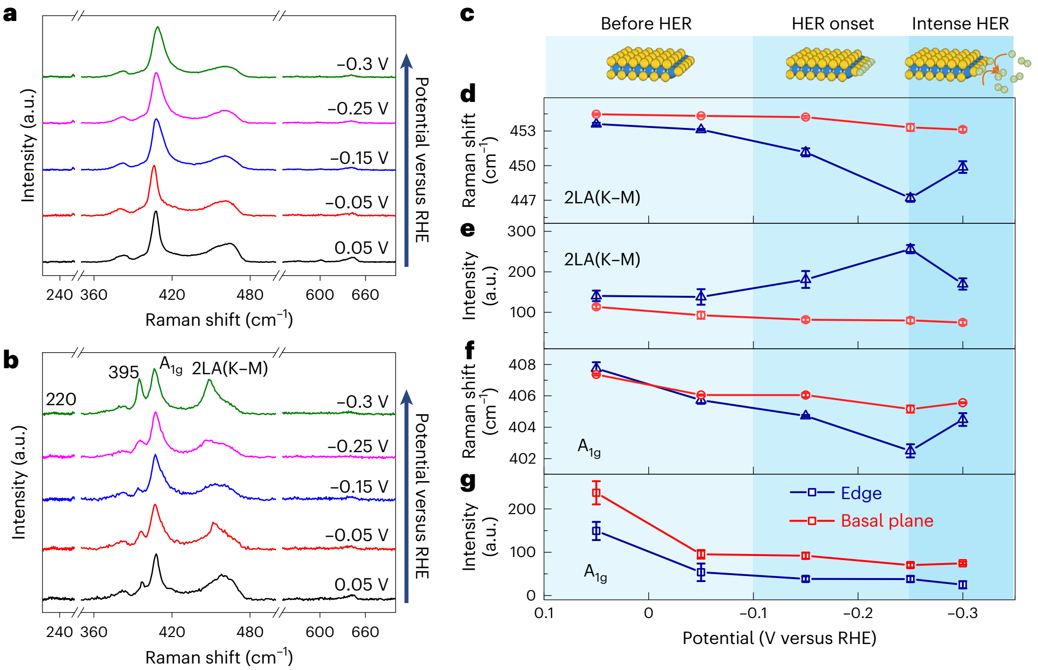

Fig. 2 | EC-TERS spectral evolution of MoS_2 during the HER. a,**b**, Potential-dependent EC-TERS of the basal plane (**a**) and edge (**b**). The spectral background is subtracted, and the intensity is normalized to the A_{1g} peak for comparison. **c**, Schematic of hydrogen coverage at the edge in different HER states. Yellow, blue and green spheres denote sulfur, molybdenum and hydrogen atoms, respectively. **d**–**g**, Potential dependence of two Raman modes: peak positions (**d**) and intensities (**e**) of the 2LA(K–M) mode, and peak positions (**f**) and intensities (**g**) of the A_{1g} mode of the edge and the basal plane. Error bars indicate that the s.d. for the three separate measurements originates from different positions along the same edge by a distance of 2 nm, with the centre being the mean. Peak positions and intensities were obtained using Lorentz fit. It should be noted that the peak position has been corrected by the tip effect (see Supplementary Note 4 for more details).

states at the saddle point along the KM direction (simply denoted as 2LA(K–M) mode), undergo an apparent evolution for both peak position and intensity (see Supplementary Fig. 3 and Supplementary Note 2 for the detailed band assignment). In principle, the energy (peak position) and amplitude (intensity) of Raman modes is determined by phonon dispersion of a certain lattice structure, and by charge density due to electron–phonon coupling[24,25]. For example, it was found that the peak position of the A_{1g} mode at ~406 cm^{-1} can be tuned by doping[26] and strain[22]. Therefore, the modified spectral behaviour at the edge during the HER originated from the response of the lattice structure and the charge density to reactions.

By contrast, neither defect-induced modes nor spectral evolution was observed under reaction conditions in confocal (that is, far-field) Raman measurements (Fig. 1d). Because the laser spot is usually around 1 µm, the defects are so small (typically several nanometres or less) that their signals are too weak to distinguish themselves from the huge background signal of the surrounding basal plane. Ex situ TERS measurement was also performed over the MoS_2 sample before and after hydrogen evolution (Fig. 1e). Under this condition, the sample was exposed to air without electrolyte and potential control. Not surprisingly, the spectral evolution occurring during in situ measurement was not observed in the ex situ measurement, indicating the surface of the electrocatalyst has relaxed to a state that is different from the one under potential control, that is, desorption of adsorbed hydrogen occurs. These control experiments clearly demonstrate the advantage and necessity of performing in situ and high spatial resolution EC-TERS measurements during the reaction process, so that the information from the edge site will not be submerged in the basal plane.

Structural evolution of the active site

From the fact that the spectral feature of the edge is sensitive but that of the basal plane is insensitive to the potential change during the reaction, we can infer that the active site for the HER is indeed the edge of MoS_2 layer, which is in accordance with the reported works[14,15]. Such information cannot be readily obtained from conventional ex situ TERS or confocal Raman measurements. Because Raman modes can reflect the geometric and electronic properties, we monitored their spectral features at a series of potentials to comprehensively study the evolution of different surface sites during HER processes. Figure 2a,b shows potential-dependent EC-TERS spectra of the basal plane and edge, respectively. Indeed, a much more obvious change can be observed at the edge than on the basal plane. To clearly see the trends, we plot peak positions and intensities of two Raman modes (that is, A_{1g} and 2LA(K–M)) versus the applied potential for both basal plane and edge sites in Fig. 2d–g.

As shown by the red curves in Fig. 2d,e, the 2LA(K–M) mode of the basal plane shows negligible variation in both peak position and intensity when the applied potentials spanned from 0.05 V to −0.3 V versus RHE. The results suggest that the 2LA(K–M) mode is insensitive to the charge density since electrons are injected into the material with the negative shift of potentials. By contrast, the blue curves in Fig. 2d,e illustrate that the same mode of the edge first remains unchanged before the HER (0.05 to −0.05 V versus RHE), but dramatically redshifts and strengthens as the HER begins (−0.15 to −0.25 V versus RHE). We performed density functional theory (DFT) calculations to understand the spectral evolution at the edges. As shown in Supplementary Table 2 and Supplementary Fig. 10, the 2LA(K–M) mode is sensitive to the lattice symmetry. In particular, the adsorption of hydrogen atoms on sulfur atoms at the edge moves the sulfur atom away from the molybdenum plane and increases the length of the molybdenum–sulfur bond, resulting in the redshifted frequency and amplified intensity of 2LA(K–M) mode (see Supplementary Note 3.2 for more details). The calculation also suggests a more notable spectral change at a higher hydrogen coverage. Therefore, before the HER (0.05 to −0.05 V versus RHE), no

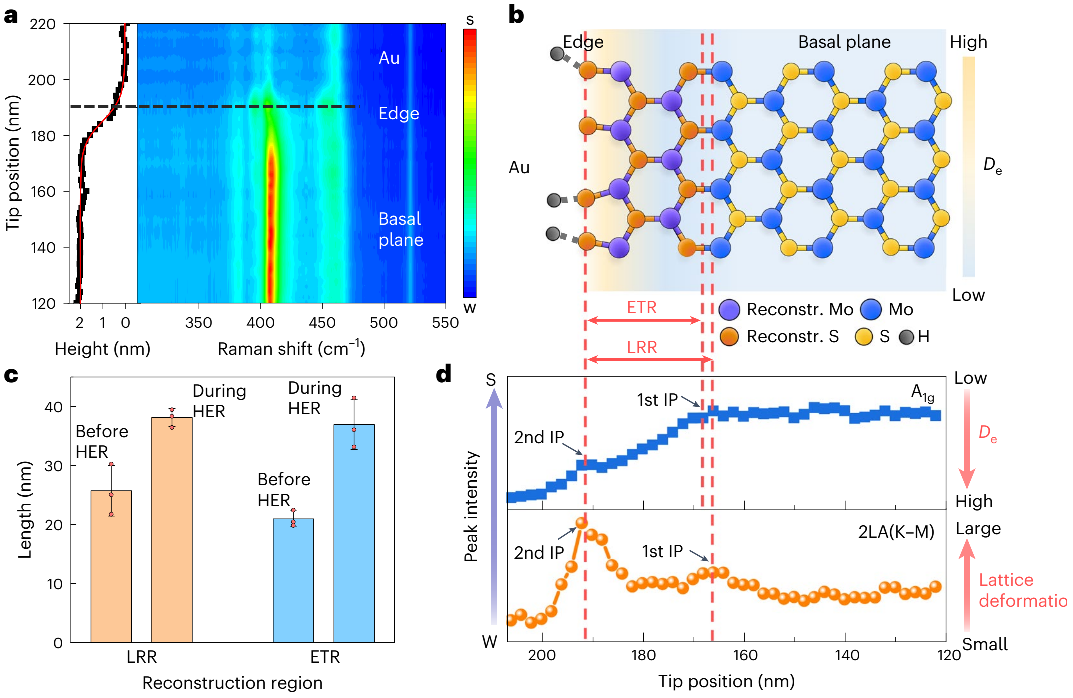

Fig. 3 | Lattice reconstruction and electronic transition regions induced by the edge. a, EC-TERS line image across the edge of a bilayer MoS_2. Left: topographic height profile of the edge. Right: colour-coded intensity map of the line-trace TERS spectra across the edge at −0.15 V versus RHE. The colour scale bar denotes the TERS intensity from weak (w) to strong (s). Note that these are original TERS experimental spectra without any data treatment. **b**, Schematic diagram of the LRR and ETR near the edge. D_e, electron density. **c**, Lengths of the LRR and ETR before (−0.05 V versus RHE) and during (−0.3 V versus RHE) the HER. The error bars show the s.d. for three parallel experiments, with the centre being the mean and dots representing reconstruction lengths from each parallel experiment. **d**, Plots of normalized intensities of two TERS peaks (A_{1g}, ~406 cm^{-1}; 2LA(K–M), ~455 cm^{-1}) with the tip position in **b**. IP, inflection point.

obvious spectral changes indicate negligible hydrogen adsorption. At −0.15 V versus RHE, protons from the acid solution start to be reduced and adsorbed at the edge[27], where the hydrogen coverage and lattice deformation increase with the negative shift of the applied potential (−0.25 V versus RHE). The adsorbed hydrogen can further react with the adjacent adsorbed hydrogen atom or the proton in the solution to produce adsorbed H_2 followed by H_2 desorption[28]. Therefore, when the potential further negatively shifts, the consumption of adsorbed hydrogen becomes so severe that the hydrogen coverage decreases. Consequently, the spectral variation reverses when the HER becomes intense at −0.3 V versus RHE, as shown in Fig. 2d,e.

Unlike the 2LA(K–M) mode, the A_{1g} mode is sensitive to both the charge density[26] and lattice structure[29,30]. Figure 2e shows the potential-dependent peak position of the A_{1g} mode at both the edge and the basal plane. The A_{1g} mode of the edge first downshifts as the potential changes from 0.05 V to −0.25 V versus RHE and then shifts to a higher frequency with a further decrease in the potential. However, the A_{1g} mode of the basal plane exhibits a slow and monotonic downshift. The difference in peak positions between the edge and the basal plane is small before the HER (0.05 to −0.05 V versus RHE) and then becomes distinct during the HER (−0.15 to −0.3 V versus RHE). Note that the adsorption of hydrogen ions results in a greater density of states near the edge (Supplementary Fig. 12). Compared with the basal plane, the edge accepts more electrons at negative potentials (Supplementary Note 3.3 and Supplementary Fig. 8), resulting in a lower A_{1g} frequency at the edge than that at the basal plane. However, the adsorption of hydrogen atoms breaks the original lattice structure of the edge (Fig. 2c, top) and subsequently modifies the A_{1g} mode vibrating along the *z* axis. Therefore, both the modified electron density and lattice deformation may explain the different trend of the edge at −0.25 to −0.3 V versus RHE compared with the basal plane. By contrast, the A_{1g} intensities at different potentials for the edge and basal plane show a similar trend, that is, both decrease with the negative shift of the potential, as shown in Fig. 2g. This result suggests that the electrode potential, which modifies the electron density, can tune the A_{1g} intensity much more effectively than the effect of hydrogen adsorption does.

The above observations demonstrate the notable influence of hydrogen adsorption on the structural properties of the edge. Owing to its larger charge density compared with the basal plane, the edge undergoes lattice deformation and exhibits decreased electron density and distortion of the molybdenum–sulfur angle. These unique structural properties facilitate hydrogen adsorption at the edge and further enhance lattice deformation.

Quantification of the lengths of the reconstruction regions

It has been demonstrated that hydrogen only adsorbs at the edge during HER processes[21,31] and modifies the geometric and electronic properties of the edge. The different intrinsic properties of the edge and the basal plane induce lattice and electronic reconstruction regions, which in turn act as active regions to enhance the hydrogen evolution activity of the edge. On the basis of the distinctive Raman response of the active edge and inactive basal plane to the applied potentials, we further used EC-TERS line imaging to explore the dynamics of the active site and visualize the synergistic evolution of atoms around it to reveal the intrinsic nature of the active sites.

Figure 3a shows a typical topographic height profile (left panel) and the corresponding colour-coded intensity map of the line-trace TERS image (right panel) of the bilayer edge marked in Fig. 1b. The line-trace TERS image of the edge matches well with the height profile. Figure 3d plots the typical intensity profiles of two TERS peaks (2LA(K–M), ~455 cm^{-1}; A_{1g}, ~406 cm^{-1}) at −0.15 V versus RHE. As shown in the bottom panel, the Raman intensity of the 2LA(K–M) mode gradually increases to the first inflection point when the tip is moved from the basal plane to the edge and then reaches the second inflection point at

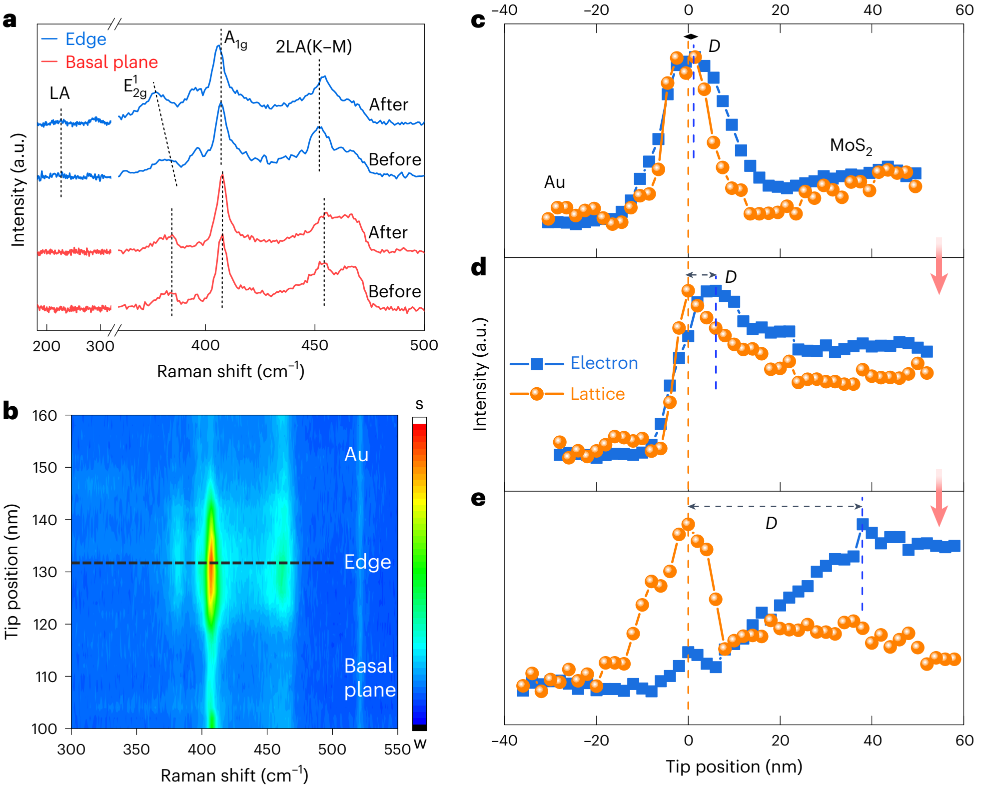

Fig. 4 | EC-TERS study of MoS$_2$ during electrochemical activation. a, TERS spectra of the bilayer edge and basal plane before and after electrochemical activation. **b**, A typical colour-coded intensity map of the line-trace TERS spectra across the edge of a bilayer MoS$_2$ before activation. The colour scale bar denotes the TERS intensity from weak to strong. **c**–**e**, Plots of normalized intensities of the electron-density-sensitive (A$_{1g}$) and lattice-structure-sensitive (2LA(K–M)) peaks with tip position: unactivated MoS$_2$ before the HER (**c**), unactivated MoS$_2$ during the HER (**d**); activated MoS$_2$ before the HER (**e**). Note that tip positions with the highest 2LA(K–M) intensities are defined as zero. The dashed lines denote tip positions with the highest A$_{1g}$ and 2LA(K–M) intensities. *D* is the distance between these two maximum values.

the edge. As a stronger 2LA(K–M) peak implies a more intense lattice deformation, the maximum lattice deformation occurs at the edge due to hydrogen adsorption. The A$_{1g}$ intensity profile also has two inflection points at a similar position as the 2LA(K–M) mode, but the total intensity fluctuation is distinct. This difference further indicates the synergistic effect of the lattice structure and charge density on the A$_{1g}$ intensity. The inflection point at the edge is because of the intrinsic electronic and geometric properties of edges, including the local electron density of states, the unsaturated coordinated defect structure and the adsorption of hydrogen atoms. The other inflection point inside MoS$_2$ can be attributed to the increase in the electron density induced by the different Fermi levels between the basal plane and the edge. Consequently, the boundary of two different electron density regions may induce lattice strain which results in lattice deformation[32] and thus the first inflection point of the 2LA(K–M) mode at a similar position.

Different lattice deformations at the edge and on the basal plane will lead to a lattice reconstruction region (LRR) between them, and the different electron densities create an electron transition region (ETR) around the active edge (Fig. 3b). Figure 3c shows the statistics of the measured lengths of LRR and ETR at potentials before (−0.05 V versus RHE) and during (−0.3 V versus RHE) the HER after removing the effect of TERS spatial resolution by deconvoluting the electromagnetic field intensity distribution under the tip (see Supplementary Note 5 for more details). Before the HER reaction, the LRR and ETR induced by the edge are 25.7 ± 4.3 nm and 21.0 ± 1.4 nm, respectively. When the HER becomes intense at −0.3 V versus RHE, the sizes of the LRR and ETR expand to 37.0 ± 4.2 nm and 38.1 ± 1.5 nm, respectively. On the one hand, the adsorption of hydrogen atoms at the edge, which is the first elemental step of the HER process, will introduce deformation of lattice structures and thus change the LRR[33]. On the other hand, the funnel effect as a result of the band bending of the basal plane near the edge and the consumption of electrons at the edge during the HER result in an increase of the ETR. Surface or structural reconstruction of active sites for metal catalysts, including changes in phase[34], coordination number[35] and compositions[36], has been reported as a result of molecular adsorption and thermal effects under reaction conditions. These changes affect the reactivity and catalytic performance[34–36]. Therefore, the variation of lattice and electronic properties around the active site is not only a passive response to reactions, but also a self-optimization of specific processes. Indeed, we conducted a Pourbaix-like analysis based on the relationship between ΔG_H and electrochemical potential for various hydrogen coverages at pH 0 to reveal the role of structural reconstruction during catalytic HER processes (Supplementary Note 3.6). The theoretical results show that the preferred hydrogen coverage for the HER decreases with the negative shift of the electrochemical potential. As a result, an atomic reconstruction (~0.5 Å) occurs predominantly at the edge and gradually diminishes over a considerable length scale across the adjacent basal plane. Both experimental and theoretical results suggest that although the edge is the local active site for the HER, the synergistic reconstructions of lattice and electron density in the region around the active site also influence the electrocatalytic performance. It is interesting to note that the atoms at/around the coordinately unsaturated edge sites tend to adjust themselves so that the resulting lattice structure has the lowest energy. With the adsorption of hydrogen atoms, the edge and the adjacent basal plane will undergo a series of structural relaxations in an energetically favourable way to reduce the activation energy of

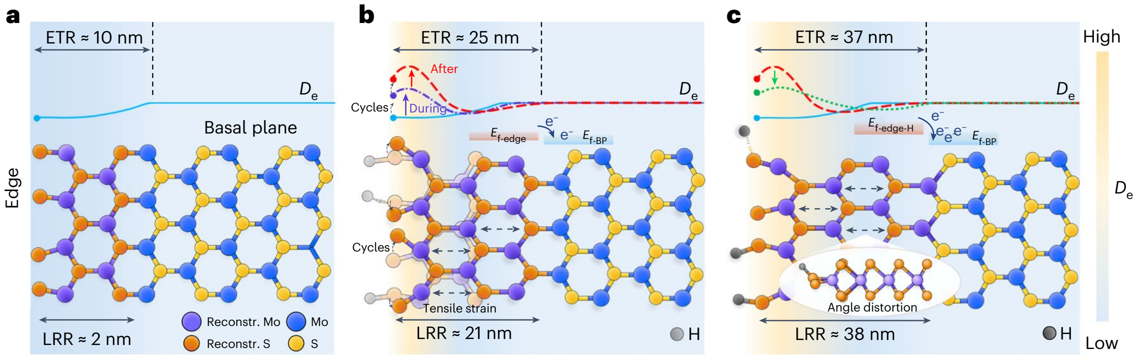

Fig. 5 | Structural evolution of the edge in atomically thin MoS_2 in different states. a, Pristine MoS_2. **b**, MoS_2 after activation. **c**, MoS_2 during HER. The four curves denote the position-dependent electron density fluctuation of MoS_2 in the pristine state (solid line), during activation (dash-dotted line), after activation (dashed line) and during the HER (dotted line). f-edge, f-BP and f-edge-H denote the Fermi level of the edge, basal plane and H-adsorbed edge, respectively.

hydrogen adsorption[2]. Such a variation of geometric structures at the active site enables a high activity in electrocatalysis.

The role of electrochemical activation

It is common practice in electrochemistry to pretreat the electrode with potential cycling or polarization at reaction potentials to enhance the electrocatalytic performance[37,38]. Similarly, we have observed that the highest and the most stable catalytic activities can be achieved after electrochemically polarizing MoS_2 at the HER potential in acidic media for some time[39,40]; the HER activity of MoS_2 was enhanced after several cycles of cyclic voltammetry (0.35 to −0.45 V versus RHE) (Supplementary Fig. 20). However, there is still no consensus on the detailed mechanism of such activation processes. In this section, we used EC-TERS to study the evolution of the active edge during the electrochemical activation process. To clearly identify the difference in the spectral features at the bilayer edge before and after electrochemical activation, we present the representative TERS spectra in Fig. 4a. The spectral features from the basal plane essentially did not change before and after activation. By contrast, the edge exhibits distinctly different Raman features for the three Raman peaks, that is, E^1_{2g} (~385 cm^{-1}), A_{1g} (406 cm^{-1}) and 2LA(K–M) (455 cm^{-1}), after the electrochemical activation, indicating a notable change in the physicochemical properties. The peak position of the E^1_{2g} mode dramatically shifts downward by ~6 cm^{-1}, indicating a large strain[41] at the edge after the activation. The tensile strain leads to a shift of defect-induced electronic bands toward the Fermi level, resulting in an increased number of gap states around the Fermi level, which strengthens hydrogen adsorption at the edge[39]. This may be the critical factor accounting for the enhanced HER activity: it has been reported that a sulfur vacancy with 1.35% tensile strain has a 1.6–2.0 times higher turnover frequency than one without strain[39]. The tensile strain also induces a lattice deformation at the edge, leading to the upshift of the 2LA(K–M) peak position, as observed in Fig. 4a. Furthermore, the downshift of the A_{1g} mode indicates an increase in the electron density at the edge after electrochemical activation, which favours cathodic reactions.

To further investigate the evolution of the reconstruction region during electrochemical activation, we performed TERS line-scan imaging of the edge during the first cycle of the activation process. Figure 4b shows a typical colour-coded intensity map of the line-trace TERS spectra across the edge of a bilayer MoS_2 before activation. We plot the normalized intensities of the A_{1g} and 2LA(K–M) peaks as a function of tip position (Fig. 4c–e) to reveal the change in LRR and ETR before and after activation. For MoS_2 (Fig. 4c) before activation (unactivated), the intensities of both peaks reach their maximum at the edge before the HER, indicating the lowest electron density at the edge, which is similar to that observed in air[16]. In comparison, there is a considerable deviation in positions of the maximum intensities for the A_{1g} and 2LA(K–M) peaks after the HER at −0.3 V versus RHE for the unactivated MoS_2, where the position of the maximum intensity of A_{1g} moves slightly toward the basal plane (Fig. 4d). Furthermore, the intensity difference of the A_{1g} peak between the edge and basal plane becomes less evident during the HER, indicating increased electron density at/near the edge. After tens of cycles of HER cyclic voltammetry treatment for electrochemical activation, the position of maximum A_{1g} intensity keeps moving into the basal plane as shown in Fig. 4e, while the position of the maximum 2LA(K–M) intensity remains at the edge with an expanded LRR.

Such a drastic and irreversible reconstruction may not only be due to the repeated adsorption and desorption of hydrogen atoms at the edge, which results in a reversible reconstruction as shown in the previous section. Theoretical findings have indicated that the adsorbed hydrogen might lead to the gradual and irreversible loss of edge sulfur atoms in the form of H_2S during the activation process[42]. Furthermore, considerable strain on the structure is induced due to the loss of sulfur atoms, creating a 'rippling' effect that extends over a long length scale. These findings align with EC-TERS observations. Furthermore, computational investigation of the lattice structure of the molybdenum edge with varying sulfur coverages (Supplementary Fig. 16) shows drastic alterations in S–Mo–S bond angles and molybdenum–sulfur bond lengths at the edge, indicating an obvious strain induced by the loss of sulfur atoms. Therefore, the loss of sulfur atoms emerges as a possible activation mechanism.

Discussion

In this work, EC-TERS was used to reveal the nanoscale evolution of the geometric and electronic properties of MoS_2 active sites (that is, edge sites) during electrochemical activation and HER processes (Fig. 5). Pristine MoS_2 has the lowest electron density at the edge due to p-type oxygen doping and the largest lattice deformation due to the unsaturated coordination structure in MoS_2 (ref. 16) (Fig. 5a). As a result, transition regions form with gradually changing electronic (ETR ≈ 10 nm) and geometric (LRR ≈ 2 nm) properties from the edge to the basal plane[16]. By shifting the potential to the HER region during the electrochemical activation cycle, hydrogen atoms bind to the edge, resulting in an increase in the tensile strain and electron density at the edge. The lattice structure cannot return to its original state while shifting the potential back to more positive values, leading to the build-up of structural deformation with the increasing activation cycles. After stabilization, an electron density reconstruction region of up to 25 nm and a lattice reconstruction region of ~21 nm form (Fig. 5b). As such a reconstructed structure is induced during the HER, which can be considered self-optimization, the catalytic activity of the edge for the HER is improved. During HER processes (Fig. 5c), the adsorbed hydrogen atoms at the activated edge further increase lattice deformation, reflected by changes in the bond angle and molybdenum–sulfur bond length, and raise the Fermi level of the edge, which facilitates electron transfer to the basal plane. The LRR and ETR expand to nearly 40 nm when the HER is intense. These observations shed light on the nature of active sites and demonstrate the advantage of in situ EC-TERS for the study of the catalytically active sites on MoS_2. The deep understanding of the active site opens promising ways toward rationally designing electrocatalysts. Future advances in optics and the fabrication of special TERS tips will further improve the enhancement and temporal-spatial resolution of EC-TERS, enabling simultaneous investigation of the interaction between the active site and molecular species (for example, catalytic intermediates) and the evolutionary dynamics of active sites.

Methods

Sample preparation

An ultrasmooth gold film was prepared following a template-stripping method[43]. First, 200 nm gold was deposited onto a clean Si(111) wafer by electron-beam evaporation (Temescal, FC-200) in a vacuum chamber at a pressure of 5×10^{-7} torr and a rate of 0.35 nm s^{-1}. Next, small glass slides were glued to the gold film using ultraviolet adhesive (Norland Optical Adhesive, NOA81). The glue was then exposed to ultraviolet light for 10–20 min. Before use, the glass slide is peeled off to expose the atomically smooth gold surface.

A natural MoS_2 single crystal with thickness of 0.3–0.5 mm was purchased from Nanjing MKNANO. MoS_2 layered samples were obtained by mechanical exfoliation[17,18] and followed by dry transfer to gold film by the Steele method[18]. In brief, freshly cleaved MoS_2 was fabricated on Nitto tape and repeatedly peeled off to reduce the thickness of MoS_2. Then, the Nitto tape was pasted onto a viscoelastic polydimethylsiloxane stamp (Gel-park, WF-20-X4), producing large numbers of thin MoS_2 flakes. The stamp was inspected under an optical microscope to select suitable MoS_2 flakes and finally pressed against the exposed gold surface to transfer the MoS_2. No doping effect from the gold substrate on MoS_2 was observed due to the existence of an ice-like water layer[16].

Tip preparation

The AFM-TERS tips used for the EC-TERS measurements were fabricated by electrochemical deposition of gold followed by atomic layer deposition (ALD) of SiO_2 onto the silicon AFM tips (NT-MDT)[19]. First, the radii of the gold TERS tips were tuned to be around 65 nm according to our reported protocol to give the highest TERS enhancement[20]. Next, the growth of a thin layer of SiO_2 (<1 nm) was conducted on a R-200 Advanced ALD system (Picosun Oy). Tris(dimethylamino)silane was used as the silicon precursor and ultrapure water was used as the oxidant. The reaction temperature was set to be 160 °C. The newly prepared TERS tips were fixed on a home-made tip-holder for the ALD process. During the reaction, the two precursors were separately injected into the reaction chamber with inert carrier gas (N_2, 99.99%; flow rate, 150 sccm). The thickness of the SiO_2 layer can be tuned by the number of reaction cycles during ALD.

EC-TERS measurement

EC-TERS experiments were performed on our home-built EC-AFM-TERS system with a top-illumination configuration[19]. This system was established on the basis of a commercial TERS set-up (NT-MDT), which combined an AFM, a confocal Raman spectroscopy and a white-light optical imaging set-up. During the EC-TERS measurements, a 60× water-immersion objective (numerical aperture, 1.0; working distance, 2 mm; Olympus) was used for both excitation and collection of the back-scattered Raman signal from the sample. A 660 nm laser with a p-polarized configuration was used for the EC-TERS measurements. SiO_2-protected gold-coated AFM-TERS tips were used to produce TERS enhancement. Contact-mode AFM was used for TERS, and tapping-mode AFM was used for measuring the topography of the sample. In the TERS line-trace imaging experiment, the tip was scanned over the sample of interest at a velocity of 2 nm s^{-1} and the TERS spectra were acquired simultaneously. All the TERS data in this work are pure near-field spectra after subtracting the far-field signal unless otherwise mentioned. The working electrode (thin layer MoS_2 on gold film), counterelectrode (platinum black ring) and the quasi-reference electrode (platinum wire) were placed in a home-made EC-TERS cell made of poly(chlorotrifluroethylene). The size of the EC-TERS cell was estimated to be around 3 cm (length) × 2 cm (width) × 0.5 cm (depth). H_2SO_4 (0.5 M) was used as the electrolyte. Potential control during the EC-TERS was achieved by a CHI660D electrochemical workstation (CH Instrument). All experiments were performed at room temperature. All chemicals used in our experiment were analytical-grade reagents. All the solutions were prepared with Milli-Q water.

Theoretical simulations

The DFT calculations were performed using the Vienna Ab Initio Simulation Package (VASP)[44]. The electron–ion interaction was described by the projector augmented wave pseudopotentials and the plane-wave basis set with a kinetic energy cut-off of 500 eV. The exchange-correlation function is described by the Perdew–Burke–Ernzerhof version of the generalized gradient approximation[45]. The conjugated gradient method was performed for geometry optimization. The convergence condition for the energy was 10^{-8} eV. The electronic and vibrational properties of the edge defect and the effect of hydrogen-atom adsorption is calculated by using a zigzag nanoribbon with a different coverage of hydrogen-atom adsorption, the details of which are discussed in Supplementary Note 3. Unit cell and nanoribbon structures were relaxed until the force on each atom was less than 10^{-2} eV Å^{-1}. Monkhorst–Pack special k-point meshes with a maximum spacing of $2\pi \times 0.01$ Å^{-1} were used for various nanoribbon structures. The phonon dispersion and vibrational density of states of nanoribbons (see Supplementary Note 3.4 for details) were calculated by using 1 × 3 × 1 supercell and based on DFT implemented in VASP software in connection with Phonopy software[46]. The effect of the solvent was treated in an implicit way using VASPsol[42] for the calculation of the Gibbs free energy, with the Debye screening length of 3 Å corresponding to the 0.5 M aqueous H_2SO_4 solutions used in the experiment[42,47]. The charge of the system varied from −0.8 to 1.6 with step of $0.2e^-$ to demonstrate the potential-dependent Gibbs free energy.

Data availability

Data that support the findings of this study are available within the paper, the Supplementary Information and the Source data files. Additional data are available from the authors upon reasonable request. Source data are provided with this paper.

References

1. Zhao, S., Yang, Y. & Tang, Z. Insight into structural evolution, active sites, and stability of heterogeneous electrocatalysts. *Angew. Chem. Int. Ed.* **134**, e202110186 (2022).
2. Li, H., Li, L. & Li, Y. The electronic structure and geometric structure of nanoclusters as catalytic active sites. *Nanotechnol. Rev.* **2**, 515–528 (2013).
3. Mefford, J. T. et al. Correlative operando microscopy of oxygen evolution electrocatalysts. *Nature* **593**, 67–73 (2021).
4. Nagashima, S. et al. Atomic-level observation of electrochemical platinum dissolution and redeposition. *Nano Lett.* **19**, 7000–7005 (2019).
5. Roeffaers, M. B. J. et al. Spatially resolved observation of crystal-face-dependent catalysis by single turnover counting. *Nature* **439**, 572–575 (2006).
6. Pfisterer, J. H. K., Liang, Y., Schneider, O. & Bandarenka, A. S. Direct instrumental identification of catalytically active surface sites. *Nature* **549**, 74–77 (2017).

7. Sambur, J. B. et al. Sub-particle reaction and photocurrent mapping to optimize catalyst-modified photoanodes. *Nature* **530**, 77–80 (2016).
8. Zeng, Z.-C. et al. Electrochemical tip-enhanced Raman spectroscopy. *J. Am. Chem. Soc.* **137**, 11928–11931 (2015).
9. Kurouski, D., Mattei, M. & Van Duyne, R. P. Probing redox reactions at the nanoscale with electrochemical tip-enhanced Raman spectroscopy. *Nano Lett.* **15**, 7956–7962 (2015).
10. Pfisterer, J. H. K., Baghernejad, M., Giuzio, G. & Domke, K. F. Reactivity mapping of nanoscale defect chemistry under electrochemical reaction conditions. *Nat. Commun.* **10**, 5702 (2019).
11. Huang, S.-C. et al. Probing nanoscale spatial distribution of plasmonically excited hot carriers. *Nat. Commun.* **11**, 4211 (2020).
12. Touzalin, T., Joiret, S., Lucas, I. T. & Maisonhaute, E. Electrochemical tip-enhanced Raman spectroscopy imaging with 8 nm lateral resolution. *Electrochem. Commun.* **108**, 106557 (2019).
13. Cao, Y. Roadmap and direction toward high-performance MoS_2 hydrogen evolution catalysts. *ACS Nano* **15**, 11014–11039 (2021).
14. Deng, J. et al. Triggering the electrocatalytic hydrogen evolution activity of the inert two-dimensional MoS_2 surface via single-atom metal doping. *Energy Environ. Sci.* **8**, 1594–1601 (2015).
15. Jaramillo, T. F. et al. Identification of active edge sites for electrochemical H_2 evolution from MoS_2 nanocatalysts. *Science* **317**, 100–102 (2007).
16. Huang, T.-X. et al. Probing the edge-related properties of atomically thin MoS_2 at nanoscale. *Nat. Commun.* **10**, 5544 (2019).
17. Novoselov, K. S. et al. Two-dimensional gas of massless Dirac fermions in graphene. *Nature* **438**, 197–200 (2005).
18. Castellanos-Gomez, A. et al. Deterministic transfer of two-dimensional materials by all-dry viscoelastic stamping. *2D Mater.* **1**, 011002 (2013).
19. Bao, Y.-F. et al. Atomic force microscopy based top-illumination electrochemical tip-enhanced Raman spectroscopy. *Anal. Chem.* **92**, 12548–12555 (2020).
20. Yang, L.-K. et al. Rational fabrication of a gold-coated AFM TERS tip by pulsed electrodeposition. *Nanoscale* **7**, 18225–18231 (2015).
21. Mitterreiter, E. et al. In-situ visualization of hydrogen evolution sites on helium ion treated molybdenum dichalcogenides under reaction conditions. *NPJ 2D Mater. Appl.* **3**, 25 (2019).
22. Mignuzzi, S. et al. Effect of disorder on Raman scattering of single-layer MoS_2. *Phys. Rev. B* **91**, 195411 (2015).
23. Sohier, T. et al. Enhanced electron–phonon interaction in multivalley materials. *Phys. Rev.* **9**, 031019 (2019).
24. Wu, J.-B., Lin, M.-L., Cong, X., Liu, H.-N. & Tan, P.-H. Raman spectroscopy of graphene-based materials and its applications in related devices. *Chem. Soc. Rev.* **47**, 1822–1873 (2018).
25. Zhang, X. et al. Phonon and Raman scattering of two-dimensional transition metal dichalcogenides from monolayer, multilayer to bulk material. *Chem. Soc. Rev.* **44**, 2757–2785 (2015).
26. Chakraborty, B. et al. Symmetry-dependent phonon renormalization in monolayer MoS_2 transistor. *Phys. Rev. B* **85**, 161403 (2012).
27. Huang, Y., Nielsen, R. J., Goddard, W. A. & Soriaga, M. P. The reaction mechanism with free energy barriers for electrochemical dihydrogen evolution on MoS_2. *J. Am. Chem. Soc.* **137**, 6692–6698 (2015).
28. Li, W. et al. Hydrogen evolution reaction mechanism on 2H-MoS_2 electrocatalyst. *Appl. Surf. Sci.* **498**, 143869 (2019).
29. Zhu, C. R. et al. Strain tuning of optical emission energy and polarization in monolayer and bilayer MoS_2. *Phys. Rev. B* **88**, 121301 (2013).
30. Kim, J. et al. Anomalous optical excitations from arrays of whirlpooled lattice distortions in moiré superlattices. *Nat. Mater.* **21**, 890–895 (2022).
31. Lunardon, M. et al. Catalytic activity of defect-engineered transition metal dichalcogenides mapped with atomic-scale precision by electrochemical scanning tunneling microscopy. *ACS Energy Lett.* **8**, 972–980 (2023).
32. Singh, A., Sharma, G., Singh, B. P. & Vasa, P. Charge-induced lattice compression in monolayer MoS_2. *J. Phys. Chem. C* **123**, 17943–17950 (2019).
33. Lechner, C., Baranek, P. & Vach, H. Adsorption of atomic hydrogen on defect sites of graphite: Influence of surface reconstruction and irradiation damage. *Carbon* **127**, 437–448 (2018).
34. Sun, J.-J. & Cheng, J. Solid-to-liquid phase transitions of sub-nanometer clusters enhance chemical transformation. *Nat. Commun.* **10**, 5400 (2019).
35. DeRita, L. et al. Structural evolution of atomically dispersed Pt catalysts dictates reactivity. *Nat. Mater.* **18**, 746–751 (2019).
36. Zugic, B. et al. Dynamic restructuring drives catalytic activity on nanoporous gold–silver alloy catalysts. *Nat. Mater.* **16**, 558–564 (2017).
37. Hu, C. et al. In situ electrochemical production of ultrathin nickel nanosheets for hydrogen evolution electrocatalysis. *Chem* **3**, 122–133 (2017).
38. Chia, X., Ambrosi, A., Sofer, Z., Luxa, J. & Pumera, M. Catalytic and charge transfer properties of transition metal dichalcogenides arising from electrochemical pretreatment. *ACS Nano* **9**, 5164–5179 (2015).
39. Xi, F. et al. Structural transformation identification of sputtered amorphous MoS_x as an efficient hydrogen-evolving catalyst during electrochemical activation. *ACS Catal.* **9**, 2368–2380 (2019).
40. Li, G. et al. Activating MoS_2 for pH-universal hydrogen evolution catalysis. *J. Am. Chem. Soc.* **139**, 16194–16200 (2017).
41. Conley, H. J. et al. Bandgap engineering of strained monolayer and bilayer MoS_2. *Nano Lett.* **13**, 3626–3630 (2013).
42. Abidi, N., Bonduelle-Skrzypczak, A. & Steinmann, S. N. How stable are 2H-MoS_2 edges under hydrogen dvolution reaction conditions? *J. Phys. Chem. C* **125**, 17058–17067 (2021).
43. Hegner, M., Wagner, P. & Semenza, G. Ultralarge atomically flat template-stripped Au surfaces for scanning probe microscopy. *Surf. Sci.* **291**, 39–46 (1993).
44. Kresse, G. & Furthmüller, J. Efficient iterative schemes for ab initio total-energy calculations using a plane-wave basis set. *Phys. Rev. B* **54**, 11169–11186 (1996).
45. Perdew, J. P., Burke, K. & Ernzerhof, M. Generalized gradient approximation made simple. *Phys. Rev. Lett.* **77**, 3865–3868 (1996).
46. Togo, A. & Tanaka, I. First principles phonon calculations in materials science. *Scr. Mater.* **108**, 1–5 (2015).
47. Steinmann, S. N. & Sautet, P. Assessing a first-principles model of an electrochemical interface by comparison with experiment. *J. Phys. Chem. C* **120**, 5619–5623 (2016).

Acknowledgements

This work was financially supported by the National Natural Science Foundation of China (NSFC) (grant numbers 22021001, 22227802, 21790354, 11874350, 92061118, 22372141 and 62374158), the National Key R&D Program of China (grant number 2023YFA1407000), the Strategic Priority Research Program of CAS (grant number XDB0460000), the Fundamental Research Funds for the Central Universities (grant number 20720220016) and the CAS Key Research Program of Frontier Sciences (grant numbers ZDBS-LY-SLH004 and XDPB22). We thank X. Yang for his assistance with theoretical discussion.

Author contributions

T.-X.H., X.W. and B.R. conceived the project. T.-X.H., S.-S.W. and Y.-F.B. performed the experiments. M.-F.C. fabricated the SiO_2-coated gold tip. X.C., J.-B.W., M.-L.L. and P.-H.T. performed the DFT calculations. L.W. helped with the experiments. T.-X.H., X.C., X.W. and B.R. wrote the manuscript. All authors participated in the analysis and discussion.

Competing interests

The authors declare no competing interests.

Additional information

Supplementary information The online version contains supplementary material available at https://doi.org/10.1038/s41929-024-01148-x.

Correspondence and requests for materials should be addressed to Xiang Wang, Ping-Heng Tan or Bin Ren.

Peer review information *Nature Catalysis* thanks Patrick Unwin, Katrin F. Domke and the other, anonymous, reviewer(s) for their contribution to the peer review of this work.